The Astrophysical Journal Letters, 924:L34 (7pp), 2022 January 10 https://doi.org/10.3847/2041-8213/ac47fa
© 2022. The Author(s). Published by the American Astronomical Society.
OPEN ACCESS

Plasma Emission Induced by Electron Beams in Weakly Magnetized Plasmas

Yao Chen[1,2], Zilong Zhang[1,2], Sulan Ni[1,2], Chuanyang Li[1,2], Hao Ning[1,2], and Xiangliang Kong[1,2]
[1] Institute of Frontier and Interdisciplinary Science, Shandong University, Qingdao, Shandong, 266237, People's Republic of China; yaochen@sdu.edu.cn
[2] Institute of Space Sciences, Shandong University, Shandong, 264209, People's Republic of China
Received 2021 August 6; revised 2022 January 2; accepted 2022 January 2; published 2022 January 18

Abstract

Previous studies on the beam-driven plasma emission process were done mainly for unmagnetized plasmas. Here we present fully kinetic electromagnetic particle-in-cell simulations to investigate this process in weakly magnetized plasmas of the solar corona conditions. The primary mode excited is the beam-Langmuir (BL) mode via classical bump-on-tail instability. Other modes include the Whistler (W) mode excited by electron cyclotron resonance instability, the generalized Langmuir (GL) waves that include a superluminal Z-mode component with smaller wavenumber k and a thermal Langmuir component with larger k, and the fundamental (F) and harmonic (H) branches of plasma emission. Further simulations of different mass and temperature ratios of electrons and protons indicate that the GL mode and the two escaping modes (F and H) correlate positively with the BL mode in intensity, supporting that they are excited through nonlinear wave–wave coupling processes involving the BL mode. We suggest that the dominant process is the decay of the primary BL mode. This is consistent with the standard theory of plasma emission. However, the other possibility of a $\mathrm{Z}+\mathrm{W}\rightarrow$ O–F coalescing process for the F emission cannot be ruled out completely.

Unified Astronomy Thesaurus concepts: Solar corona (1483); Solar activity (1475); Radio bursts (1339); Solar coronal radio emission (1993); Plasma astrophysics (1261)

Supporting material: animations

1. Introduction

The standard plasma emission (PE) mechanism, first proposed more than six decades ago (Ginzburg & Zheleznia-kov 1958), is a multistage, nonlinear process including: (1) efficient excitation of Langmuir (L) turbulence by electron beams through the kinetic bump-on-tail instability, (2) scattering of Langmuir waves by ion-acoustic (IA) wave or ion-density inhomogeneities to generate the fundamental (F) O-mode radiation and/or backward-propagating Langmuir waves, noted as $\mathrm{L}\pm\mathrm{IA}\rightarrow$ O–F and $\mathrm{L}\pm\mathrm{IA}\rightarrow\mathrm{L}'$, and (3) resonant coupling of forward- and backward-propagating Langmuir turbulence to generate harmonic (H) radiation, noted as $\mathrm{L}+\mathrm{L}'\rightarrow\mathrm{H}$. Extensive studies on PE have been carried out with the original theoretical framework being largely maintained (e.g., Melrose 1980, 1987; Cairns 1987; Robinson et al. 1994; Schmidt & Cairns 2012; Li & Cairns 2013, 2014; Schmidt & Cairns 2012, 2014; Thurgood & Tsiklauri 2015; Che et al. 2017; Henri et al. 2019).

Despite significant progresses, it is very challenging to verify the complete PE mechanism with PIC simulation, partially due to limits of computational resources since such a simulation should adopt a large enough domain and long enough duration so as to support relevant wave modes. The frequency of the fundamental emission of the O mode is at or very close to its cutoff around the plasma oscillation frequency ($\sim\omega_{\mathrm{pe}}$). This corresponds to a small wave number and a long wavelength. The IA mode, determined by the ion dynamics, has a relatively low frequency (and a long period). In addition, the simulation is necessarily multidimensional to consider the wave coupling process, and the number of macroparticles per cell should be as large as possible so as to reduce the noise level. With these constraints, earlier studies present inconclusive or even contradictory statements regarding whether and which of the proposed PE processes occur in their simulations. Thurgood & Tsiklauri (2015) presented a critical review on these earlier studies, pointing out that some studies did not conduct the convergence test and/or disentangle contributions from non-escaping electromagnetic modes, thus the relevant PE process has not been conclusively verified.

Thurgood & Tsiklauri (2015) concluded that simulations with a dense beam ($n_{\mathrm{b}}/n_0\sim$0.05, the density ratio of the beam to background electrons) prohibit the L+IA $\rightarrow$ O–F process while those with a dilute beam ($n_{\mathrm{b}}/n_0\sim 0.0057$) allow such a process. This is in line with the dispersion analysis of the beam-plasma system (Cairns 1989) that indicates mismatch of the coalescence conditions in the presence of a dense beam. This point has been used to explain why some earlier studies fail to verify the complete PE process.

Thurgood & Tsiklauri (2015) demonstrated the excitations of the F and H emissions from a single-beam plasma system via fully kinetic PIC simulations, in accordance with the standard PE theory. Yet, it is questionable whether the simulation time is long enough and the domain is large enough to simulate the low-frequency IA and the long-wavelength O–F emission. Their study does not take the magnetization effect into account. This is equivalent to assuming that the plasma emission process is unaffected by the magnetization effect and waves such as the Whistler (W) mode and the so-called electromagnetic superluminal Z mode are irrelevant.

Henri et al. (2019), however, found that the F emission in their simulation is hardly discernible though they did adopt a dilute beam with a spatial domain (simulation time) larger (longer) than that of Thurgood & Tsiklauri (2015), within a similar unmagnetized beam-plasma system.

Original content from this work may be used under the terms of the Creative Commons Attribution 4.0 licence. Any further distribution of this work must maintain attribution to the author(s) and the title of the work, journal citation and DOI.

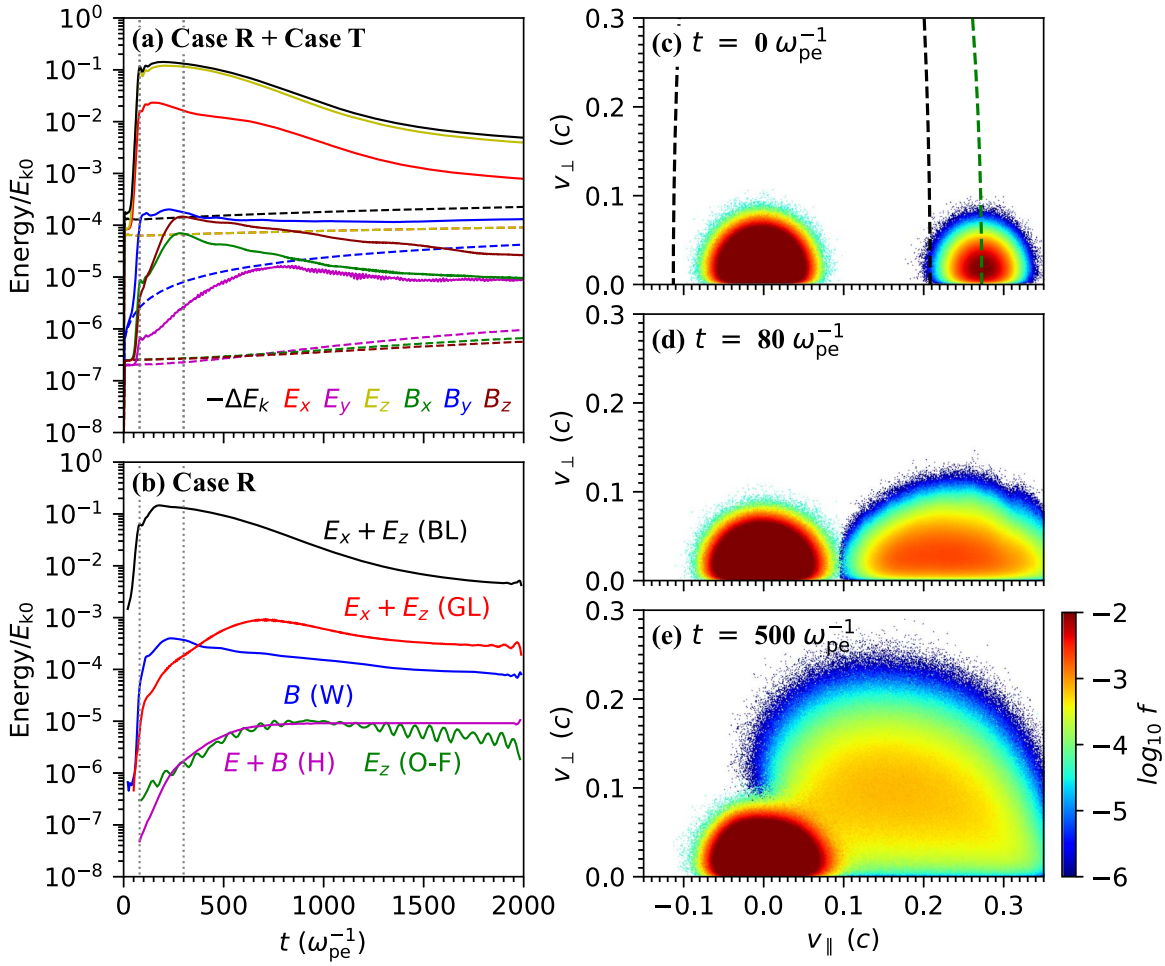

Figure 1. (a) Energy variations of the six field components and the negative change of the total electron energy ($-\Delta E_k$) for Case R (solid lines) and Case T (dashed lines); (b) energy variations of specific field components of various wave modes for Case R (BL for the beam-Langmuir mode, W for Whistler, O–F for the fundamental, and H for the harmonic PE); panels (c)–(e) illustrate the VDFs at three moments. Overplotted in panel (c) are two resonance curves of the W mode with the following (ω, k, θ) values: [0.1 Ω_{ce}, 4.5 Ω_{ce}/c, 30°] and [0.3 Ω_{ce}, 12.3 Ω_{ce}/c, 60°]. The two dashed lines in panels (a)–(b) represent $t = 80\ \omega_{pe}^{-1}$ and $t = 300\ \omega_{pe}^{-1}$.

The latest theoretical studies extended earlier analysis on the kinematics of electrostatic Langmuir decay from unmagnetized to magnetized plasmas (Layden et al. 2013; Cairns & Layden 2018) and found that such decay is always kinematically permitted and can proceed for very fast streams and generate Langmuir waves with very small wave numbers that are the Z-mode component of the so-called generalized Langmuir mode (GL) in magnetized plasmas (see, e.g., Melrose 1986; Willes & Cairns 2000). This removes the kinematic constraints from earlier unmagnetized theory and may affect the evolution of the beam-plasma system and relevant PE process. The predicted decay process has yet to be verified with PIC simulations.

According to recent PIC simulations of PE for weakly magnetized plasmas energized by energetic electrons with loss-cone-type distributions (Ni et al. 2020; Li et al. 2021), the fundamental O-mode (O–F) emission can be generated through the coalescence of the almost counter-propagating Z and W modes that are excited through the electron cyclotron resonance instability (ECMI). Follow-up studies verified the occurrence of such a Z + W → O–F process through the wave-pumping method of PIC simulation (Ni et al. 2021). It is intriguing to figure out whether the W and Z modes and their coalescing process can occur in a magnetized beam-plasma system.

Thus, it is necessary to conduct PIC simulations of the beam-plasma interaction in magnetized plasmas to verify the occurrence of the above Langmuir decay process and to clarify the role of electromagnetic modes such as W and Z in generating PEs. This is the main purpose of the present study.

2. Simulation Method and Parameter Setup

The beam-plasma system was simulated with the open-source Vector PIC (VPIC) code on supercomputers operated by the Beijing Super Cloud Computing Center. It is a fully kinetic electromagnetic and relativistic code released by the Los Alamos National Labs, run in two spatial dimensions (x, z) with three velocity components using periodic boundary conditions (Bowers et al. 2008a, 2008b, 2009). The background magnetic field is set to be $\boldsymbol{B}_0(=B_0\hat{e}_z)$, and the wave vector $\boldsymbol{k}$ is in the xOz plane. The plasmas consist of three components, including background electrons and protons with a Maxwellian distribution, and an electron beam with the following velocity distribution function (VDF, see Figure 1(c))

$$f_e = A_e \exp\left(-\frac{u_\perp^2}{2u_0^2} - \frac{(u_\parallel - u_d)^2}{2u_0^2}\right), \quad (1)$$

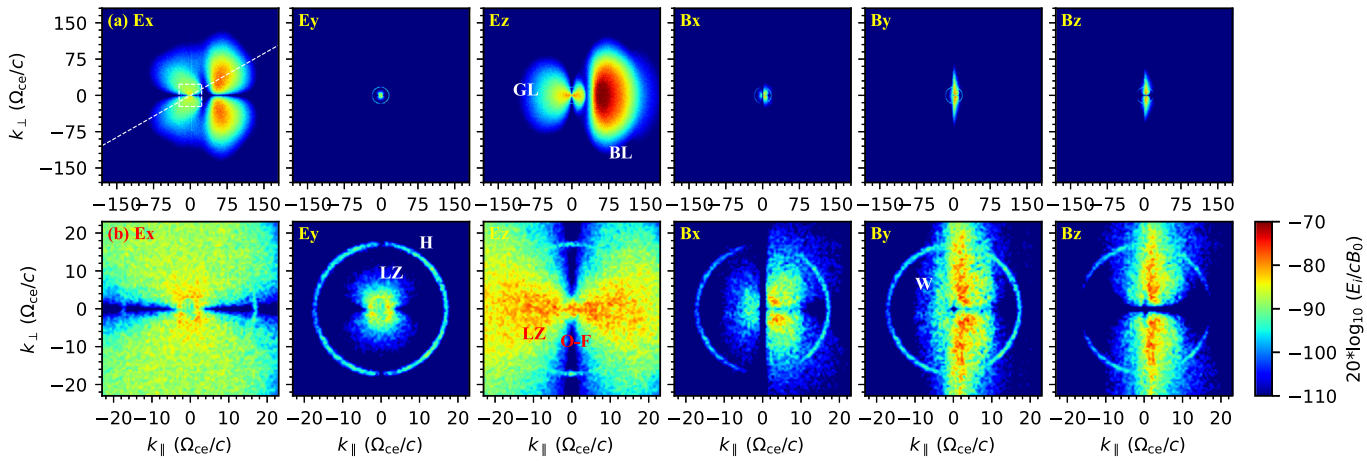

Figure 2. Intensity maps of the six field components in the wave-vector $\boldsymbol{k}$ space for Case R. Right columns of panels are the zoomed-in version of the square region plotted in the top-left panel. The dashed line indicates the propagation angle of ($\theta = 30°$) along which the ω, k dispersion maps are plotted in Figure 3.

where $u_\parallel$ and $u_\perp$ are the parallel and perpendicular components of the momentum per mass, u_0 is the thermal velocity of energetic electrons, and A_e is the normalization factor. The density ratio of beam-background electrons is set to be 0.01. All particles distribute homogeneously in space initially. The drift speed of the electron beam is set to be $u_d = 0.2824c$ (20 keV) and the ratio of ω_{pe}/Ω_{ce} to be 10. These parameters are consistent with the general conditions of the solar corona.

The domain of the simulation is taken to be $L_x = L_z = 2048\,\Delta$, where the grid spacing $\Delta = 3.25\,\lambda_{de}$, λ_{de} is the Debye length of the background electrons. The simulation lasts for 2000 ω_{pe}^{-1}. The resolvable range of $|k|$ is [0.52, 535] Ω_{ce}/c, and the range of ω is [0.04, 32] Ω_{ce} (for the time interval of 1500 ω_{pe}^{-1}). The number of macroparticles per cell is taken to be 2000 for the background electrons and 1000 for both protons and the beam. A zero-current condition is maintained initially.

3. Results and Analysis

We first present details of wave excitation for the reference case (Case R) with realistic proton-electron mass ratio ($m_p/m_e = 1836$) and equal temperature ($T_p = T_e = 2$ MK); then we compare these results with other cases of different m_p/m_e and T_p/T_e to shed light on the role of ion-related perturbations and physical connection among various wave modes.

3.1. Wave Analysis for Case R

We first present the energy profiles of various field components for Case R, in panel (a) of Figure 1, overplotted by those for the corresponding thermal case (Case T), to show the significance of wave growth in the unstable beam-plasma system. All field components of Case R are stronger in energy than those of the thermal case by at least 2–4 orders of magnitude; further analysis on energy profiles of individual wave modes (panel (b)) verifies their significant enhancements over the corresponding thermal noise signals. This is important since in PIC simulations, numerical noises organize themselves as signals along dispersion curves that might be mistaken as wave excitation (see Thurgood & Tsiklauri 2015).

According to the energy profiles, we split the whole simulation into three stages (see Figures 1(a)–(c)): 0–80 ω_{pe}^{-1} for Stage I characterized by the rapid rise of E_x and E_z in energy, corresponding to the growth of the primary BL mode, 80–300 ω_{pe}^{-1} for Stage II characterized by the gradual rise of B_x and B_z associated with the excitation of the Whistler (W) mode, and 300–1500 ω_{pe}^{-1} for Stage III corresponding to the saturation and gradual damping of various wave modes. At the end of Stage I, the value of $-\Delta E_k$ is about 12% of E_{k0}, which increases slightly to the maximum at $\sim$150 ω_{pe}^{-1}, then declines gradually as a result of the return of wave energy to electrons. In panel (b) of Figure 1, we plot the energy variation of specific field component of different wave modes, as will be discussed later.

Panels (c)–(e) present VDF maps of electrons for Case R at $t = 0$, 80, and 500 ω_{pe}^{-1}. During 0–80 ω_{pe}^{-1} (Stage I), the beam electrons are decelerated causing the rapid rise of E_x and E_z, and diffuse toward larger $v_\perp$ later. Note that similar behavior of VDF diffusion (toward larger $v_\perp$) has been indicated by Harding et al. (2020) and Melrose et al. (2021) in terms of 3D generalization of the beam-plasma interaction. They concluded that electrons can diffuse significantly in angle and thus form broad distribution similar to that illustrated here (rather than forming a plateau of VDF as implied by the previous 1D picture). The VDF does not change significantly after $\sim$500 ω_{pe}^{-1}.

In Figure 2, we present the wave-energy maps in the wave-vector ($\boldsymbol{k}$) space of the six electric ($\boldsymbol{E}$) and magnetic ($\boldsymbol{B}$) field components for Case R. The maps show the intensity maxima of waves at corresponding $\boldsymbol{k}$. The nature of the modes can be easily identified from the analytic dispersion curves plotted in Figure 3 and the accompanying movie. The strongest feature is carried by E_z (panel (c)), corresponding to the primary forward-propagating electrostatic BL mode that is excited via the well-known bump-on-tail instability. The BL mode extends $\sim\pm 60°$ away from the parallel direction with significant perpendicular component E_x. In panels (a) and (c), the two secondary wave enhancements distribute along one smooth dispersion curve, which represents the so-called generalized Langmuir (GL) mode with two components: the backward-propagating thermal Langmuir (LT) waves with larger k and the Z-mode (LZ) component with smaller k. The angular patterns of the two

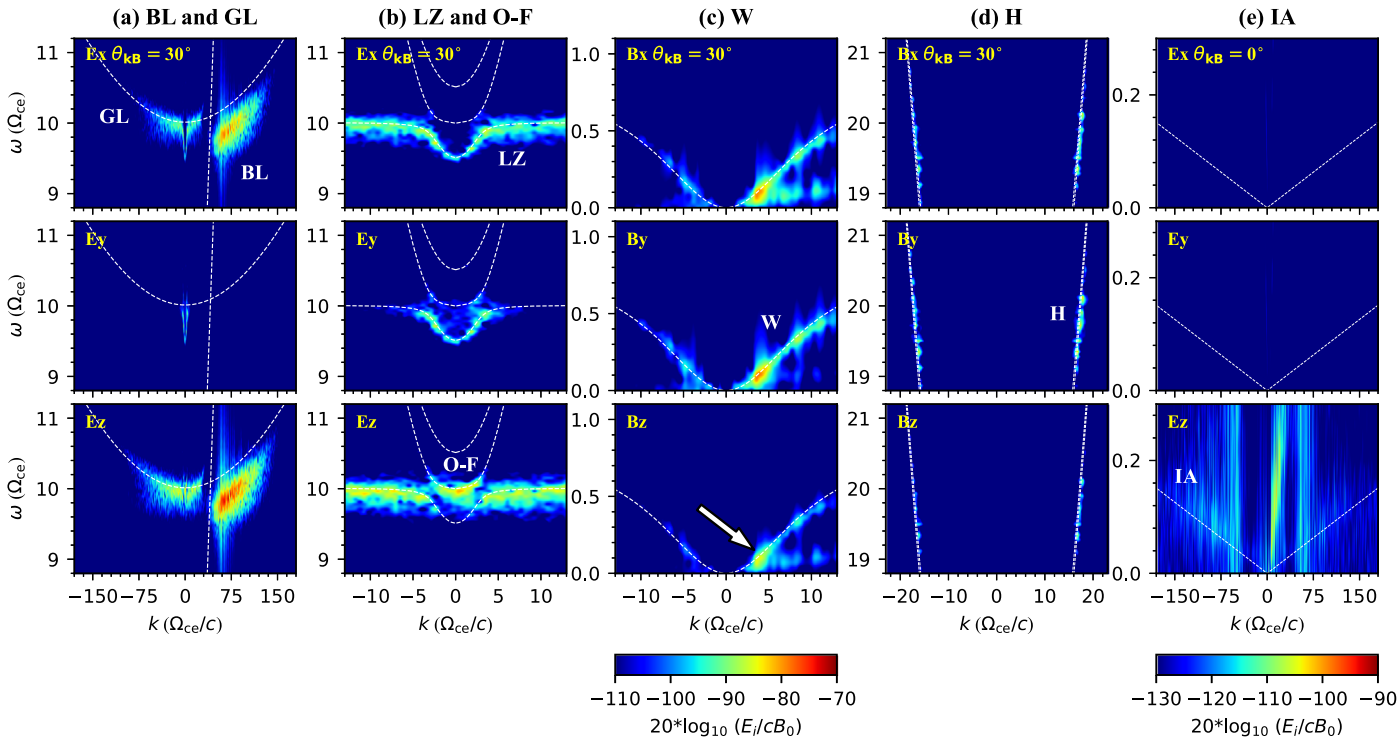

Figure 3. Dispersion diagrams of (E_x, E_y, E_z) for the BL (a), GL and O–F modes (b), those of (B_x, B_y, B_z) for the W (c) and H modes (d), and those of (E_x, E_y, E_z) for the IA mode. Overplotted lines are corresponding dispersion curves given by the magnetoionic theory. The straight dashed line in panel (a) represents the beam mode. The arrow indicates the spectral location selected to plot the resonance curve (Figure 1) for $\theta = 30°$ (see Figure 1(d)) for the W mode. The video begins at $\theta = 0°$ and advances 5° at a time up to $\theta = 90°$. The real-time duration of the video is 5 s.

(An animation of this figure is available.)

components (LT and LZ) are similar to that of the primary BL wave.

Significant enhancements on the $\boldsymbol{B}$ dispersion map are mainly associated with the W mode. The nice circular pattern represents the harmonic (H) radiation. In the middle part of the E_y dispersion, the enhanced features with low k correspond to the mixture of the electromagnetic LZ mode and the fundamental O-mode (O–F) emission. It is not possible to separate them with this type of dispersion.

In Figure 3, we present the ω–k dispersion analysis along propagation angles (θ) with strong wave enhancement. As mentioned, this figure should be combined with Figure 2 to tell the mode properties. The left column of panels (a) shows the strongest BL mode, within the ω–k range of [9.0, 10.5] Ω_{ce} and [40, 150] Ω_{ce}/c. As seen from panels (a) and (b), the GL mode exists in the range of [9.6, 10] Ω_{ce} and [−20, 20] Ω_{ce}/c for its Z-mode component and [10, 10.4] Ω_{ce} and [−90, −20] Ω_{ce}/c for its thermal component, and the O–F mode appears in the range of [−5, 5] Ω_{ce} and [10, 10.2] Ω_{ce}/c.

The O–F mode is mainly carried by the parallel electric field E_z and the LZ mode by E_x and E_z. Both modes present signatures in E_y due to their electromagnetic nature and both have phase speeds larger than c. Note that the overplotted dashed lines are dispersion curves given by the classical cold plasma magnetoionic theory. The good correlation indicates that the thermal effect is not important to the two superluminal modes.

As seen from the third row of panels (c), the W mode is also strongly excited. To demonstrate its excitation mechanism, we plot two sets of resonance curves of the ECMI process onto Figure 1(c). Both curves pass through the positive gradient region of the beam distribution, which supports the theory that it is excited via ECMI. Note that the exact growth rates depend on an integral along the resonance ellipse with an integrand that depends on the partial derivatives of the VDF with respect to both parallel and perpendicular velocity. The W mode is dominated by the three magnetic-field components. The energy profile of this mode (Figure 1(b)) rises rapidly during the early stage of the beam-plasma interaction, similar to that of the BL mode, which also supports the theory that it is excited directly. Note that according to Starodubtsev et al. (1999) and An et al. (2017), in plasmas with a large ω_{pe}/Ω_{ce}, the W mode can be directly excited through the ECMI process with $n = 1$ where n represents the harmonic number of ECMI, rather than the Landau resonance with $n = 0$. This is consistent with our analysis.

The fourth row of panel (d) presents the H emission, corresponding to the circular patten in Figure 2. Its (ω and k) ranges are [19.8, 20.2] Ω_{ce} and [17, 18] Ω_{ce}/c. According Figure 1(b), the total field energy of the H emission is about the same as that of the E_z energy of the O–F emission.

We examine the temporal development of various wave modes with energy curves for specific field component(s) (see Figure 1(b)), which are calculated by integrating field energy within a specified spectral range along the corresponding dispersion curve according to Parseval's theorem. The BL mode presents the strongest and fastest growth during the first stage, the W mode gets excited at a slower pace mainly in the second stage, and the GL mode grows gradually with time. Both PE modes (O–F and H) grow gradually before reaching the saturation level, similar to the energy profile of the GL mode.

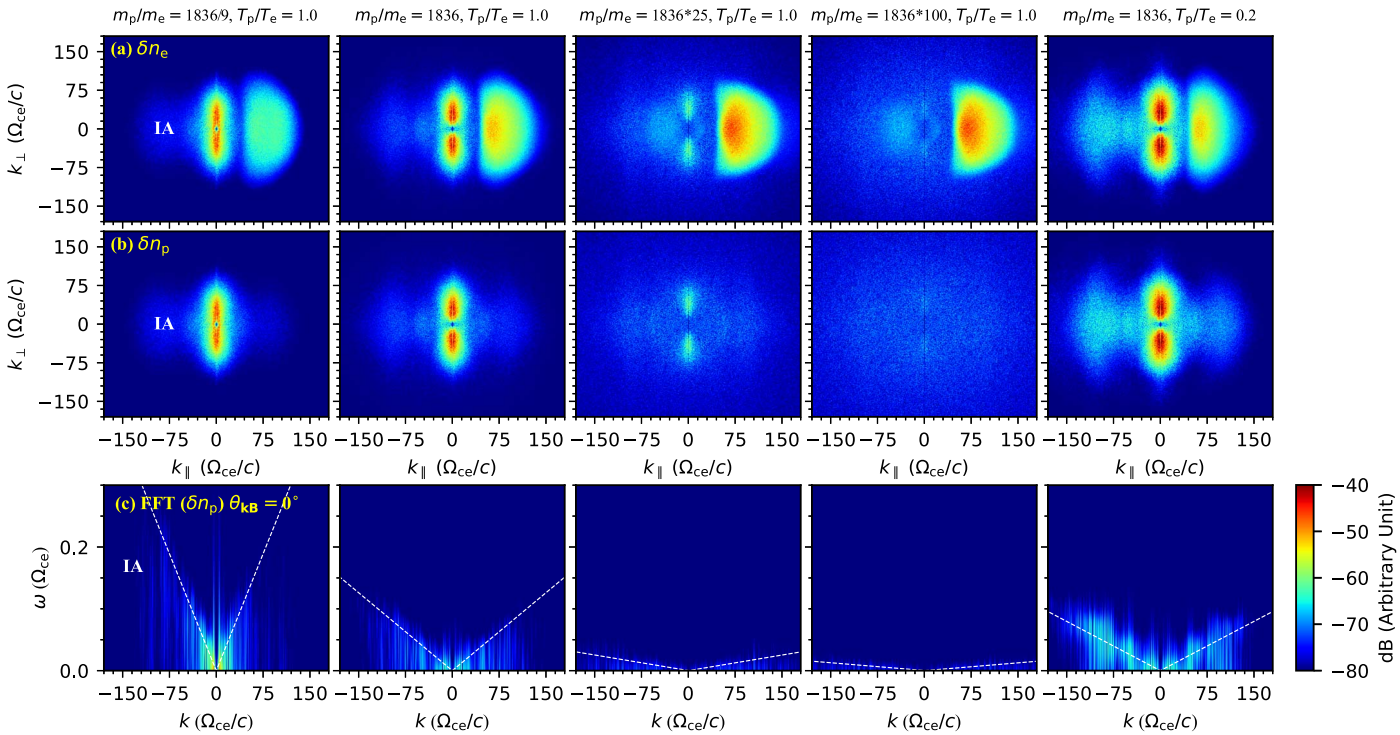

Figure 4. The Fourier spectra in the $\boldsymbol{k}$ space for density fluctuations of electrons (δn_e) and protons (δn_p). The bottom panels are for the low-frequency regime of the (ω, k) spectra; overplotted dashed lines are the standard IA dispersion relation.

We also checked the resonance curves of the GL mode and the two PE modes (not shown). Only a minor part of the GL mode has resonance curves passing through the VDF region of positive gradient, meaning that this mode cannot be excited directly through ECMI. For the O–F and H emissions, the resonance curves either do not exist (no solutions to the matching equation) or could not pass through any region of positive gradient of VDF. Therefore, neither the two PE modes can be excited via ECMI. This agrees with the standard mechanism that PEs in plasmas with $\omega_{pe}/\Omega_{ce} \gg 1$ involve a nonlinear process of three-wave coupling.

To further explore the excitation mechanism of GL and the two PE modes, we present the dispersion relation of the IA mode (see panel (e) of Figure 3), where bidirectional features of wave enhancements exist along the standard dispersion curve of IA. Note that due to the limited simulation time and spatial domain, the IA mode can at most be marginally resolved with Case R. This hinders further analysis.

3.2. Wave Analysis for Cases with Different m_p/m_e and T_p/T_e

Significant excitations of LZ and PE (O–F and H) modes are the most important result of the study. To dig out the underlying physics, we conducted additional numerical experiments with $m_p/m_e(=1836/9,\ 1836\times 25,\ 1836\times 100)$ and $T_p/T_e(=1)$ and another case with $T_p/T_e = 0.2$ and $m_p/m_e = 1836$. The solutions are presented in Figures 4 and 5. In Figure 4 we show the Fourier spectra in the wave-vector space for density fluctuations of electrons (δn_e) and protons (δn_p). The bottom panels are for the low-frequency regime of the (ω, k) spectra. In this regime, the two species have identical spectra so only those for protons are presented. Figure 5 (and the accompanying movie) presents the ω–k spectra along the selected propagating direction to illustrate the intensities of the BL mode, the GL mode including its LZ and LT components, and the O–F mode. The W mode spectra do not change much with the two ratios, thus they are not shown.

As seen from Figure 4, the main difference between the two sets of spectra is the presence of a high-frequency electrostatic BL mode in the δn_e spectra. The other features belong to low-frequency fluctuations associated with protons with charge neutrality being well maintained. In Figure 4, the major feature of the $\boldsymbol{k}$-space spectra with $m_p/m_e = 1836$ and $1836/9$ is the vertical wave enhancement which is the quasi-perpendicularly propagating IA mode (coupled with the cyclotron motion). These features are separated from the BL mode by about 30 Ω_{ce}/c in $k_\parallel$, therefore they could not participate in the three-wave coupling process involving the BL mode to generate the LZ and the O–F modes whose k values are in general less than 10 Ω_{ce}/c.

Two additional weaker features of IA exist along the parallel (anti-parallel) to oblique propagating direction, which (along with the above quasi-perpendicular mode) become invisible in cases with $m_p/m_e > 1836\times 25$ since their frequency is too low to be resolved. Note that with $T_p/T_e = 1$, the IA may be dissipated by Landau damping, thus cannot grow to stronger levels. To verify this, we conducted another simulation with $T_p/T_e = 0.2$ and $m_p/m_e = 1836$.

Comparing Figures 4 and 5, we made two observations. (1) The three modes (BL, GL, and O–F) get stronger with increasing m_p/m_e if $m_p/m_e \leqslant 1836\times 25$; in other words, the two modes (GL including its LZ and LT components and O–F) correlate positively in intensity with BL. This reveals the underlying physical connection between BL and GL/O–F; if m_p/m_e is further increased to 1836×100 then these modes do not change anymore, while the IA features disappear completely. (2) Comparing Case R with the $T_p/T_e = 0.2$ case reveals that the IA mode gets stronger for smaller T_p/T_e (due to weaker damping effect), yet the BL and GL modes remain at

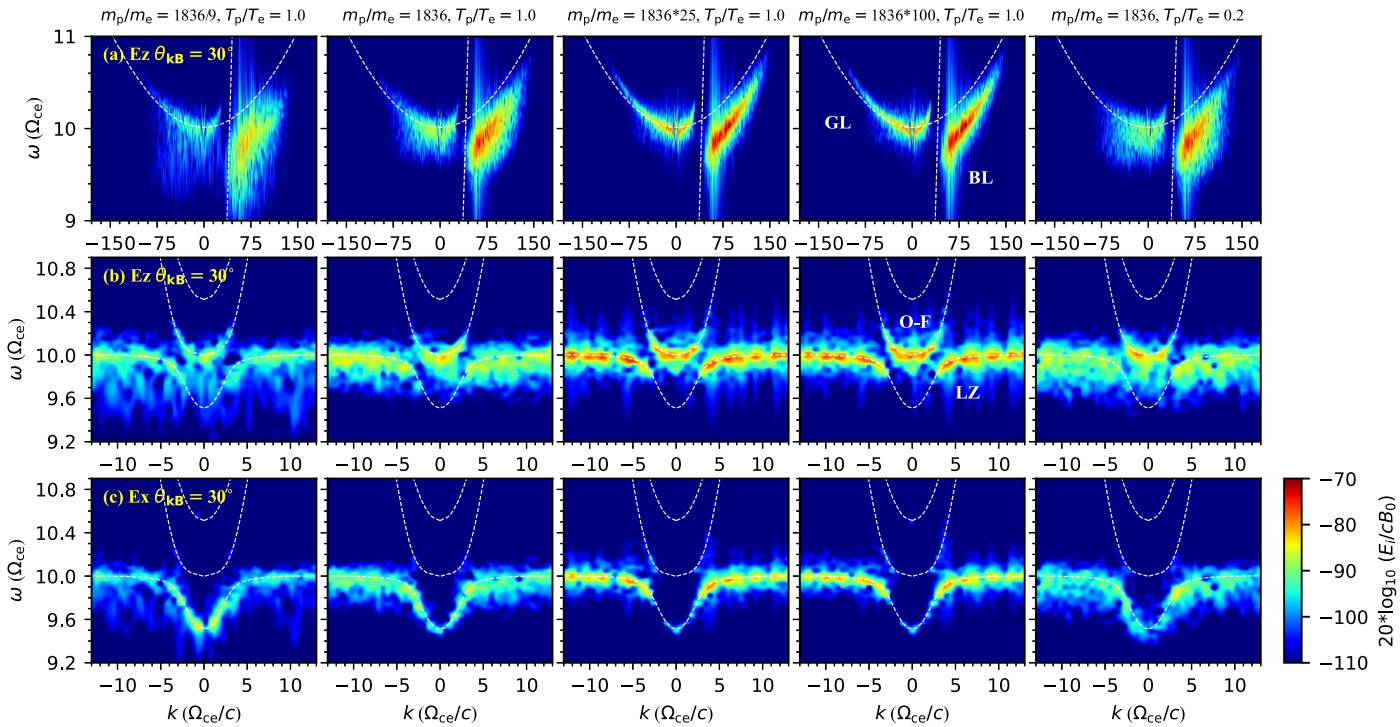

Figure 5. The ω–k spectra along selected propagating directions to illustrate the dispersion relation and intensity distribution of the BL, GL, and O–F modes. The video begins at $\theta = 0°$ and advances 5° at a time up to $\theta = 90°$. The real-time duration of the video is 5 s.

(An animation of this figure is available.)

levels close to those of Case R while the O–F mode manifests weak enhancement along the quasi-parallel to oblique propagating direction.

4. Conclusions and Discussion

This study presents fully kinetic electromagnetic PIC simulations of the interaction of a beam of energetic electrons with weakly magnetized plasmas that are characterized by solar coronal conditions. The main purpose is to investigate wave excitation and the plasma emission mechanism. Waves that are directly excited include the forward-propagating beam-Langmuir (BL) mode via the bump-on-tail instability and the Whistler (W) mode via cyclotron resonance instability. Waves that are excited through nonlinear wave–wave interactions include the generalized Langmuir (GL) mode that consists of the superlunimal Z-mode component at small wave numbers and the backward-propagating thermal component at large wave numbers. In addition, significant excitation of the O-mode fundamental (O–F) and harmonic (H) plasma emissions are also observed.

Our simulations support that the d (decay) process (BL–IA) of the primary BL mode plays a key role in generating both components of the GL mode (the LZ component at smaller k and the LT component at larger k) and the O–F emission, while the u (coalescence) process (BL + IA) may not be important here. This argument is based on the following three aspects: (1) the three modes (BL, GL, and IA) are observed in simulations for reasonable ion masses and ion temperatures, (2) the two modes (GL and O–F) correlate positively with the BL wave in intensity, and (3) they maintain a strong level even in the absence of IA, and do not get enhanced significantly when the IA mode is enhanced.

The present study provides the first demonstration of the generation of the Langmuir-Z mode in terms of the decay of the primary beam-driven Langmuir wave in weakly magnetized plasmas, using a fully electromagnetic PIC simulation. This agrees with the latest theoretical extension of the Langmuir decay process from unmagnetized to magnetized plasmas by Layden et al. (2013) and Cairns & Layden (2018) who deduced that earlier constraints on such processes should be removed when including the magnetization effect.

According to the standard PE theory, the H emission is generated by the coalescence of the primary Langmuir wave and the backward-propagating secondary Langmuir wave (L + L → H). In our terms, the process should be expressed as BL + LT → H, i.e., coalescence of the beam-Langmuir mode and the backward-propagating thermal extension of the induced GL mode. Examining Figures 3–5, we found that the corresponding matching conditions of ω and $\boldsymbol{k}$ can be easily satisfied. Thus, we suggest that the present study supports the standard PE theory of H emission.

The slight enhancement of the O–F mode with increasing IA intensity along the quasi-parallel to oblique propagating direction, as shown by comparing Case R with the ($T_p/T_e = 0.2$) case, may indicate that the coalescence of the BL and the IA mode may occur and partially contribute to the O–F emission. In addition, an alternative generation mechanism of this mode—developed recently by Ni et al. (2020, 2021) and Li et al. (2021) with the same VPIC program for magnetized plasmas yet energized by energetic electrons with the loss-cone type distribution—suggests that the O–F emission is generated via resonant coupling of almost counter-propagating Z and W modes, i.e., the Z + W → O–F process. They provided evidence of direct excitation of the Z mode, and demonstrated the match of the coalescing conditions. Ni et al.

(2021) verified the occurrence of such a process through dispersion analysis and the wave-pumping PIC simulation. In the present system, we cannot reject or support the occurrence of this process since both Z and W modes are excited and the Z mode can propagate its correlation with the primary BL mode to the O–F mode through the suspected $Z + W \rightarrow$ O–F process to be in accordance with the above observations. In other words, this process may also play a role here. Whether the two mechanisms of the fundamental PE indeed work together and if so, how much each contributes, remains unaddressed.

This study is supported by NNSFC grants (11790303 (11790300), 11973031, and 11873036). The authors acknowledge Dr. Quanming Lu, Xinliang Gao, and Xiaocan Li for helpful discussions, the anonymous referee for valuable comments, the Beijing Super Cloud Computing Center (BSC-C, URL:http://www.blsc.cn/) for computational resources, and LANL for the open-source VPIC code.

ORCID iDs

Yao Chen https://orcid.org/0000-0001-6449-8838
Hao Ning https://orcid.org/0000-0001-8132-5357
Xiangliang Kong https://orcid.org/0000-0003-1034-5857

References

An, X., Bortnik, J., Van Compernolle, B., Decyk, V., & Thorne, R. 2017, PhPl, 24, 072116
Bowers, K. J., Albright, B. J., Bergen, B., et al. 2008a, in SC'08: Proc. 2008 ACM/ Conf. on SupercomputingIEEE, 0.374 Pflop/s Trillion-Particle Kinetic Modeling of Laser Plasma Interaction on Roadrunner (New York: IEEE Press), 63
Bowers, K. J., Albright, B. J., Yin, L., et al. 2009, JPhCS, 180, 012055
Bowers, K. J., Albright, B. J., Yin, L., Bergen, B., & Kwan, T. J. T. 2008b, PhPl, 15, 055703
Cairns, I. H. 1987, JPlPh, 38, 169
Cairns, I. H. 1989, PhFlB, 1, 204
Cairns, I. H., & Layden, A. 2018, PhPl, 25, 082309
Che, H., Goldstein, M. L., Diamond, P. H., & Sagdeev, R. Z. 2017, PNAS, 114, 1502
Ginzburg, V. L., & Zhelezniakov, V. V. 1958, SvA, 2, 653
Harding, J. C., Cairns, I. H., & Melrose, D. B. 2020, PhPl, 27, 020702
Henri, P., Sgattoni, A., Briand, C., Amiranoff, F., & Riconda, C. 2019, JGRA, 124, 1475
Layden, A., Cairns, I. H., Li, B., & Robinson, P. A. 2013, PhRvL, 110, 185001
Li, B., & Cairns, I. H. 2013, JGRA, 118, 4748
Li, B., & Cairns, I. H. 2014, SoPh, 289, 951
Li, C., Chen, Y., Ni, S., et al. 2021, ApJL, 909, L5
Melrose, D. 1980, SSRv, 26, 3
Melrose, D. B. 1986, Instabilities in Space and Laboratory Plasmas (Cambridge: Cambridge University Press)
Melrose, D. B. 1987, SoPh, 111, 89
Melrose, D. B., Harding, J., & Cairns, I. H. 2021, SoPh, 296, 42
Ni, S., Chen, Y., Li, C., et al. 2020, ApJL, 891, L25
Ni, S., Chen, Y., Li, C., et al. 2021, PhPl, 28, 040701
Robinson, P. A., Cairns, I. H., & Willes, A. J. 1994, ApJ, 422, 870
Schmidt, J. M., & Cairns, I. H. 2012, JGRA, 117, A04106
Schmidt, J. M., & Cairns, I. H. 2014, JGRA, 119, 69
Starodubtsev, M., Krafft, C., Lundin, B., & Thévenet, P. 1999, PhPl, 6, 2862
Thurgood, J. O., & Tsiklauri, D. 2015, A&A, 584, A83
Willes, A. J., & Cairns, I. H. 2000, PhPl, 7, 3167